Production of radioactive beams of francium

G. Stancari[a,*], S. Veronesi[b], L. Corradi[c], S.N. Atutov[a], R. Calabrese[a], A. Dainelli[c], E. Mariotti[b], L. Moi[b], S. Sanguinetti[d], L. Tomassetti[a]

[a]*Dipartimento di Fisica and INFN, 44100 Ferrara FE, Italy*
[b]*Dipartimento di Fisica and INFM, 53100 Siena SI, Italy*
[c]*INFN Laboratori Nazionali di Legnaro, 35020 Legnaro PD, Italy*
[d]*Dipartimento di Fisica, INFM and INFN, 56127 Pisa PI, Italy*

Abstract

We describe the production of francium beams from the fusion–evaporation reaction ^{197}Au(^{18}O, kn)$^{215-k}$Fr generated by a $\sim$100 MeV ^{18}O^{6+} beam on a thick gold target. The physics of the production process is discussed, together with estimates of expected production rates. The production target is heated to $\sim$1200 K and kept at a potential of $+3$ kV to enhance Fr diffusion and surface desorption, and to accelerate surface-ionized ions. Details are given on its design and construction. The performance of the target is measured as a function of primary beam energy and flux, target temperature and extraction voltage. Average production rates are 0.7×10^6 ions/s for ^{210}Fr with a primary beam flux of 10^{12} particles/s, with peaks of 2×10^6 ions/s. From these measurements, information on the efficiency of the release processes is inferred.

1. Introduction

A cold cloud of rare atoms is desirable in several fields. Doppler-free spectroscopy of poorly-known atomic levels and measurements of fundamental interactions in atomic systems are examples of studies pursued in laboratories around the world [1,2].

Francium is particularly suitable because it is the heaviest alkali metal and it has several isotopes with relatively long lifetimes. Also, one expects enhanced parity-violating effects and reduced theoretical uncertainties from isotope comparisons [3,4]. By accumulating rare atoms in a trap, one partially compensates for their scarcity. Our group and the one at SUNY Stony Brook, who pioneered the field [5–10], are focusing on the isotopes with mass numbers in the range 208–211, and especially on ^{210}Fr.

A production target, a beam transport line and a magneto-optical trap (MOT) are operating at LNL, the national laboratories of the *Istituto Nazionale di Fisica Nucleare* (INFN) in Legnaro, Italy. An overview of our work is given in Refs. [11–14]. In this paper, we focus on the physics of francium production.

2. Production method

Francium has no stable isotopes. Its longest-lived isotope is ^{223}Fr with a half-life $T_{1/2} = 21.8$ min. It has to be produced either by nuclear decay [15,16] or by induced nuclear transmutation.

We produce francium in the mass range $208 \leqslant A \leqslant 211$ via fusion of ^{18}O and ^{197}Au and successive evaporation of neutrons from the compound nucleus: ^{197}Au(^{18}O, kn)$^{215-k}$Fr

Gold is chosen because it is mono-isotopic and chemically inert. Its melting point (1337 K) is relatively low, so that diffusion of nuclei produced inside the target

can be greatly enhanced by heating it to about 1200 K without damage. Moreover, the work function of gold (5.1 eV [22]) is higher than francium's first ionization energy (4.07 eV [15,23]). According to Langmuir's surface-ionization efficiency, practically all Fr released from the gold surface is in ionic form and can be accelerated and injected into the secondary beam line for transport to the trap cell.

The oxygen beam is accelerated to 95–115 MeV by the Tandem-XTU accelerator. Its size and position on target can be adjusted with a magnetic quadrupole and a magnetic steerer. The beam is observed through the fluorescence induced on a retractable Macor disk positioned a few centimeters upstream of the target.

The most-abundantly produced isotope is $A = 210$. The expected maximum yield is $4.4 \times 10^6 (^{210}\text{Fr ions})/\text{s}$ for an incoming flux of 10^{12} particles/s, as shown in detail in the following Section.

3. Estimates of expected yield

The observed yield Y depends on the fusion–evaporation production rate P and on the combined extraction efficiency ε of the following processes: diffusion in the target bulk (ε_d), surface desorption (ε_s), surface ionization (ε_i), and transport to a catcher foil where the ions are detected (ε_t): $Y = P \cdot \varepsilon_d \cdot \varepsilon_s \cdot \varepsilon_i \cdot \varepsilon_t \equiv P \cdot \varepsilon$.

The contribution dP to the production rate in a small target thickness dt can be calculated from the incident ^{18}O flux j, the number density n of the target nuclei, and the cross-section σ : $dP = j \cdot n \cdot \sigma \cdot dt$. In terms of the mass density $\rho = nM/N_A$ ($M = 196.96655$ g/mol is the molar mass of gold and N_A is Avogadro's constant) and of the mass thickness $dx = \rho \cdot dt$, one obtains

$$dP = j \cdot \sigma \cdot dx \cdot \left(\frac{N_A}{M}\right).$$

As the beam penetrates into the target, its energy E' decreases, and the cross-section σ and stopping power $\langle dE/dx \rangle$ vary, while the flux can be taken as constant. Our best estimate of the normalized production rate for each isotope is, therefore,

$$\frac{P}{j} = \int_0^{E_0} \frac{\sigma}{\langle dE/dx \rangle} \, dE' \cdot \left(\frac{N_A}{M}\right) \quad (1)$$

where E_0 is the initial beam energy.

A 1 μA beam of $^{18}\text{O}^{6+}$ corresponds to a flux $j = 10^{12}$ particles/s. The stopping power $\langle dE/dx \rangle$ of oxygen in gold is taken from Ziegler's tables [17,18]. It decreases from 1.9 MeV · cm²/mg at 60 MeV to 1.4 MeV · cm²/mg at 120 MeV. The fusion–evaporation cross-sections σ are calculated with the HIVAP code, which incorporates the barrier-passing model and the standard statistical model [19,20] (Fig. 1). Recently, calculations for $^{18}\text{O} + ^{197}\text{Au}$ were checked against experimental data [21].
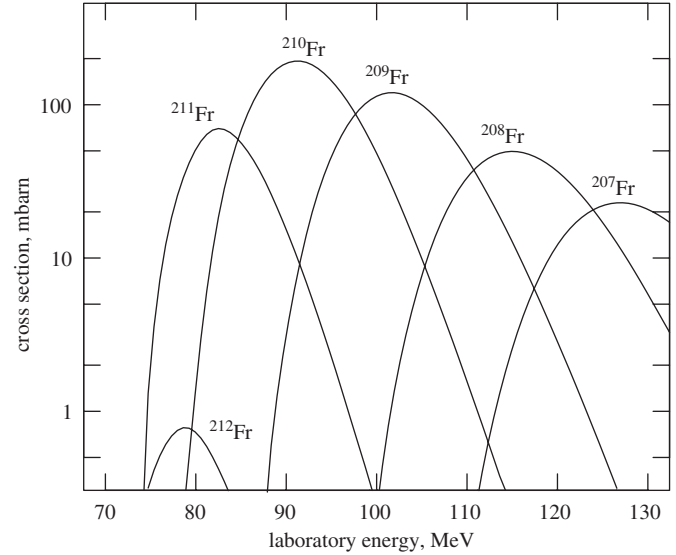

Fig. 1. Calculated fusion–evaporation cross-sections [21].
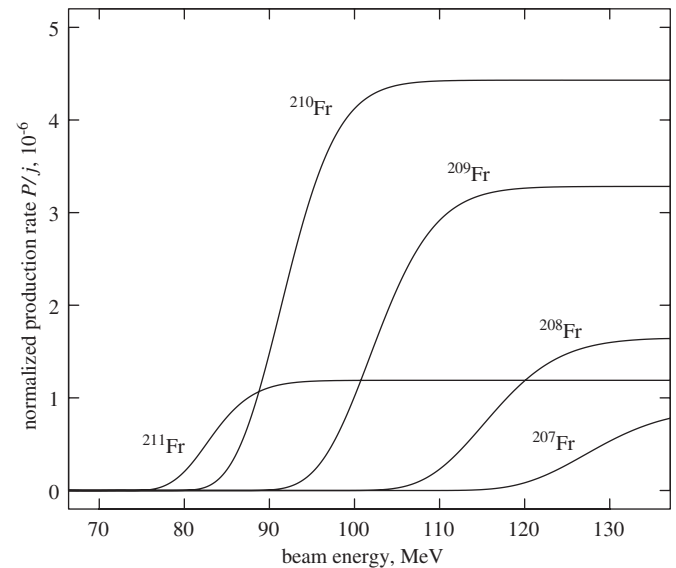

Fig. 2. Calculated francium production rates (Eq. (1)).

Fig. 2 and Table 1 give the expected production rates (Eq. (1)) of some francium nuclei as a function of oxygen beam energy E_0, for an incident flux $j = 10^{12}$ particles/s. The theoretical uncertainty on these estimates is approximately 20%.

The maximum yield does not necessarily correspond to the maximum production rate. Higher bombarding energies exploit a larger fraction of the excitation curve, but production takes place deeper inside the target bulk. Temperature strongly influences the diffusion process, as well as surface desorption and ionization. Optimal operating conditions are to be found experimentally. The above estimates provide upper limits on the attainable yields.

Table 1
Calculated francium production rates (Eq. (1)), for $j = 10^{12}$ particles/s

Energy E_0 (MeV)	Production rate P (Hz)			
	^{208}Fr	^{209}Fr	^{210}Fr	^{211}Fr
82		2.3×10^1	2.2×10^4	4.3×10^5
86		7.6×10^1	3.8×10^5	8.9×10^5
90		5.7×10^3	1.5×10^6	1.1×10^6
94	1.8×10^0	1.2×10^5	2.9×10^6	1.2×10^6
98	2.1×10^1	6.0×10^5	3.9×10^6	1.2×10^6
102	3.1×10^3	1.5×10^6	4.3×10^6	1.2×10^6
106	4.7×10^4	2.4×10^6	4.4×10^6	1.2×10^6
110	2.3×10^5	2.9×10^6	4.4×10^6	1.2×10^6
114	5.9×10^5	3.2×10^6	4.4×10^6	1.2×10^6
118	1.8×10^6	3.2×10^6	4.4×10^6	1.2×10^6

Fig. 3. Drawing of the target assembly.

4. Target assembly

The target operates at a relatively-high voltage (3 kV) and at a temperature near the melting point of gold (typically, 1200 K). It is necessary to heat it efficiently and to control its temperature at beam powers up to 25 W, while guaranteeing electrical insulation from the surrounding vacuum chamber.

The target is obtained by melting 1.5 g of gold (99.9999% purity) under vacuum (10^{-6} mbar) on a 8.65 mm-diameter, 90 mm-long tungsten rod, on the end of which a dovetail joint is previously machined to ensure good mechanical and thermal contact (Fig. 3). Once solid, the gold drop is pressed on the rod with a hammer and then machined to flatten and smoothen its surface, obtaining a 1 mm-thick gold disk of the same diameter as the tungsten rod.

The tungsten rod is anchored to a Macor post with a stainless-steel belt. The Macor post ensures thermal and electrical insulation between the target and the floor of the grounded scattering chamber. The post rests on a stainless-steel bar, which can be slid to center the target inside the vacuum chamber and align it with the incoming beam and the transport line (Fig. 4). Alignment is done with a He–Ne laser beam reflected on a mirror rigidly fixed to the target frame.

The tungsten rod is part of the heating system. It fits inside a cylindrical shell made from Shapal, a machinable ceramic with high resistivity up to 2100 K and good thermal conductivity. A tungsten heating wire (0.3 mm in diameter) is wound around the cylindrical shell. The coil is anti-inductive to suppress the magnetic field. The whole assembly is enclosed inside two molybdenum heat shields. The heater provides an approximate power of $50 \text{ V} \times 6 \text{ A} = 0.3 \text{ kW}$. The ac power supply is insulated from the coil by a 1-to-1 transformer, to prevent discharge damage. When the target is hot, the residual pressure inside the chamber is 4×10^{-7} mbar.

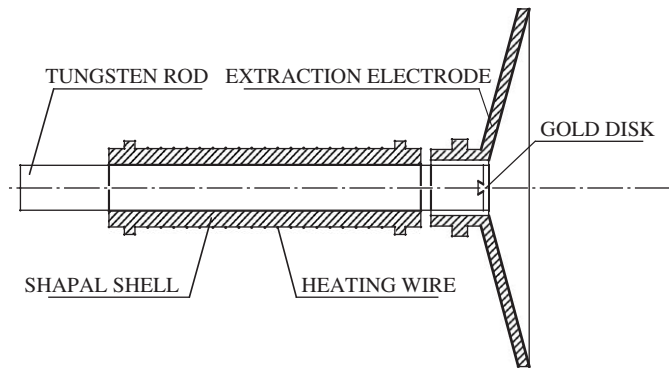The average target temperature is measured with an optical pyrometer (Impac IP1). The pyrometer is calibrated
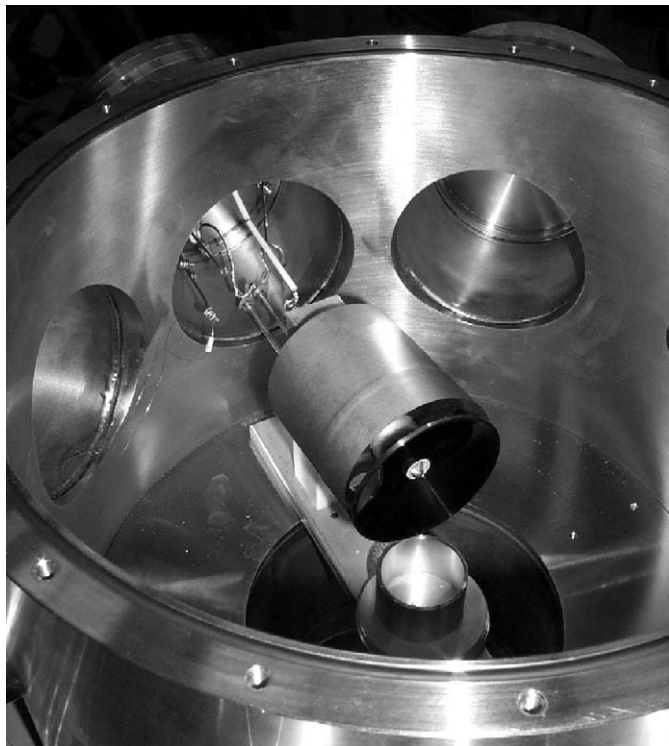

Fig. 4. Photograph of the target inside the vacuum chamber. The gold disk is at the center of the conical extraction electrode. The tungsten rod and the heater are inside the cylindrical molybdenum heat shield.

with a thermocouple when the target is at ground potential. Temperature measurements have an estimated relative uncertainty of about 2%. The target surface is also monitored with a video-camera to prevent overheating and to check temperature inhomogeneities induced by the primary oxygen beam.

The gold disk is surrounded by a stainless-steel conical extraction electrode. The electrode's outer diameter (68.7 mm) and opening angle (75°) are chosen to maximize the transport efficiency of ions to the exit of the target chamber after acceleration. The electrode is to be kept as small as possible to reduce the thermal flow and to leave room for other devices in the chamber. For simplicity, the

electrode is kept at the same electrical potential as the target assembly. The ion optics has been designed with the aid of computer program SIMION 3D [24], which calculates potentials (relaxation method) and ion trajectories, based upon electrode shapes defined on a discrete grid. The calculated beam emittance after a 3 kV acceleration is 12 and $46\,\pi$ mm mrad for an oxygen-beam 99% radius of 1 and 4 mm, respectively.

5. Measurements of production yield

We have performed experiments with several targets at different energies, fluxes, and temperatures. There is usually more than one data point for each target. When measurements taken in similar conditions are combined, the median is shown and the error bars reflect the dispersion of the data (from the 0.159 percentile to the 0.841 percentile, for a standard 68% coverage).

The production yield is measured by identifying the α decays of francium (Table 2). A retractable aluminum catcher foil intercepts the ion beam 555 mm downstream of the target (Fig. 5). The catcher's normal forms an angle of 135° with the beam direction.

A silicon surface-barrier detector (SSBD, Ortec BU-016-150-100) is used to detect α particles from the decays of Fr nuclei implanted on the catcher's surface. The detector is

calibrated with a composite α source (^{239}Pu, ^{241}Am and ^{244}Cm). In our setup, the SSBD has a geometric acceptance

$$a = \frac{1}{4\pi}\frac{(150\,\text{mm}^2)}{(73\,\text{mm})^2} = 2.2 \times 10^{-3}$$

largely independent of beam size, as estimated with the Monte Carlo technique.

The output of the SSBD is shaped and amplified (Silena 205 preamplifier and Silena 7611/L amplifier). The unipolar output of the amplifier is connected to an Ortec AD413A voltage-sensitive ADC. The flow of digitized readings is piloted by a CES 2110 CAMAC crate controller connected to a Jorway 411 highway driver. The data-acquisition system is controlled by a personal computer running GNU/Linux (RedHat 7.1) through its SCSI port (ASUS SC-200 host adapter with Symbios 53C810 chip). The CAMAC routines are based on the FNAL `sjy` package [26].

Fig. 6 shows a typical α spectrum. Decays of francium and of daughter nuclei are visible. The α particles from ^{208}Fr and ^{209}Fr have an energy difference of 5 keV and cannot be resolved by our system. The same is true for ^{210}Fr and ^{211}Fr, with an energy difference of 9 keV.

The francium yield Y of each isotope is proportional to the observed steady-state event rate S after correcting for the α decay fraction f and for the geometric acceptance a of the SSBD: $Y = S/(f \cdot a)$.

The decay fractions of ^{208}Fr and ^{209}Fr are almost equal. Moreover, the ^{208}Fr production rate is expected to be relatively small over a wide range of energies. The total yield can therefore be measured directly:

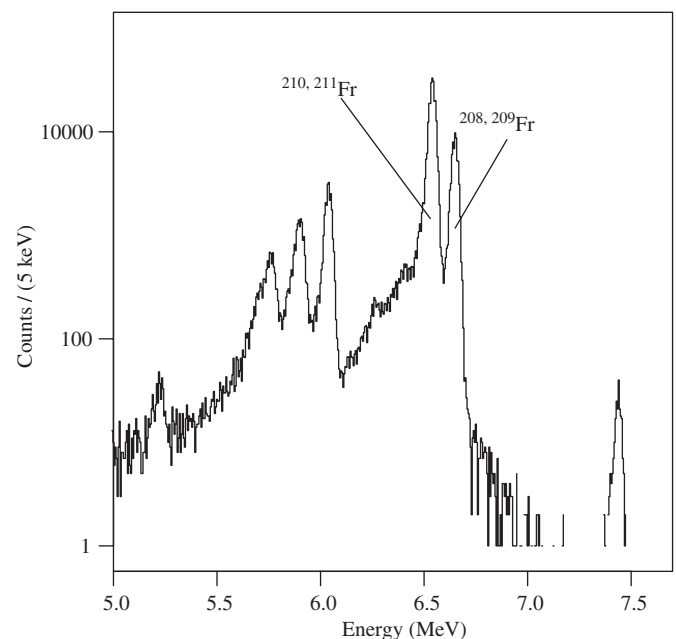$$Y_{208} + Y_{209} = \frac{(S_{208} + S_{209})}{f_{209} \cdot a}.$$

Table 2
Decay properties of selected Fr isotopes [25]. Only the most intense lines of ^{212}Fr are shown

Isotope	Half life (s)	α fraction (%)	α energy (keV)
^{207}Fr	14.8 ± 0.1	95 ± 2	6768 ± 3
^{208}Fr	59.1 ± 0.3	90 ± 4	6641 ± 3
^{209}Fr	50.0 ± 0.3	89 ± 3	6646 ± 5
^{210}Fr	191 ± 4	60 ± 30	6543 ± 5
^{211}Fr	186 ± 1	> 80	6534 ± 5
^{212}Fr	1200 ± 36	43 ± 2	$\begin{cases} 6262 \pm 2 \\ 6383 \pm 2 \\ 6406 \pm 2 \end{cases}$

Fig. 5. Experimental setup for measurements of production yield.

Fig. 6. Sample α spectrum.

We are also interested in estimating the yield of ^{210}Fr. For this, decay fractions $f_{210} = 0.6$ and $f_{211} = 0.9$ are assumed. We also rely on the relative production rates calculated with HIVAP (Section 3), under the hypothesis (tested below) that the release efficiencies of ^{210}Fr and ^{211}Fr are the same:

$$Y_{210} = \frac{P_{210}}{a} \frac{(S_{210} + S_{211})}{f_{210} \cdot P_{210} + f_{211} \cdot P_{211}}.$$

Due to these assumptions, this measurement has a larger systematic uncertainty.

In Fig. 7 the measured normalized yields $(Y_{208} + Y_{209})/j$ and Y_{210}/j are plotted as a function of primary beam energy and compared with production estimates $(P_{208} + P_{209})/j$ and P_{210}/j. We deduce that the average extraction efficiency

$$\varepsilon \equiv \frac{Y_{208} + Y_{209}}{P_{208} + P_{209}}$$

is $(15 \pm 9)\%$ above 1200 K. Similar values are obtained for Y_{210}/P_{210}.

From the data in Fig. 7, one can see that the yields are lower than the expected rates by a factor that does not depend appreciably on beam energy. This is an indication that there is a negligible difference in the diffusion of the four isotopes. A further conclusion can be drawn— the diffusion process is efficient. In fact, in our experiments, the variations in production depth of a single isotope for different primary-beam energies are comparable with the

differences in production depth among isotopes at fixed energy.

More information on the efficiency of the diffusion process comes from the study of the relative intensity of the observed ^{208,209}Fr peak

$$R \equiv \frac{(S_{208} + S_{209})}{(S_{208} + S_{209}) + (S_{210} + S_{211})}.$$

This ratio is plotted in Fig. 8 as a function of primary beam energy. In this isotope ratio, the atomic and ionic features of production (surface desorption and ionization, transport) should cancel out. In fact, we do not observe any dependence of the isotope ratio on target temperature or voltage.

The predicted ratio is also plotted

$$R^{(\text{pred})} \equiv \frac{f_{208} \cdot P_{208} + f_{209} \cdot P_{209}}{f_{208} \cdot P_{208} + f_{209} \cdot P_{209} + f_{210} \cdot P_{210} + f_{211} \cdot P_{211}}$$

with $f_{208} = 0.90$, $f_{209} = 0.89$, $f_{210} = 0.60$, and $f_{211} = 0.90$. The fact that the predicted curve reproduces the data indicates that there is a negligible difference in the diffusion of the four isotopes. Their diffusion time is short compared to their lifetime, at least over distances of the order of the difference in production depth. In terms of the diffusion coefficient of Fr in polycrystalline Au at temperatures above 1000 K, one obtains $D \gg (3\,\mu\text{m})^2/(50\,\text{s}) = 2 \times 10^{-9}\,\text{cm}^2/\text{s}$.

The oxygen beam energy is deposited locally on the gold surface, on a volume of approximately 2 mm in diameter and 30 μm deep. If the heater is properly calibrated, local melting is observed, which yields maximum Fr production for a few hours without damaging the target. Under these conditions, the extraction efficiency can reach 40%. However, most of the time we have operated in a safer regime. In our experience, the target can be used for several days at 1200 K before a replacement is required.
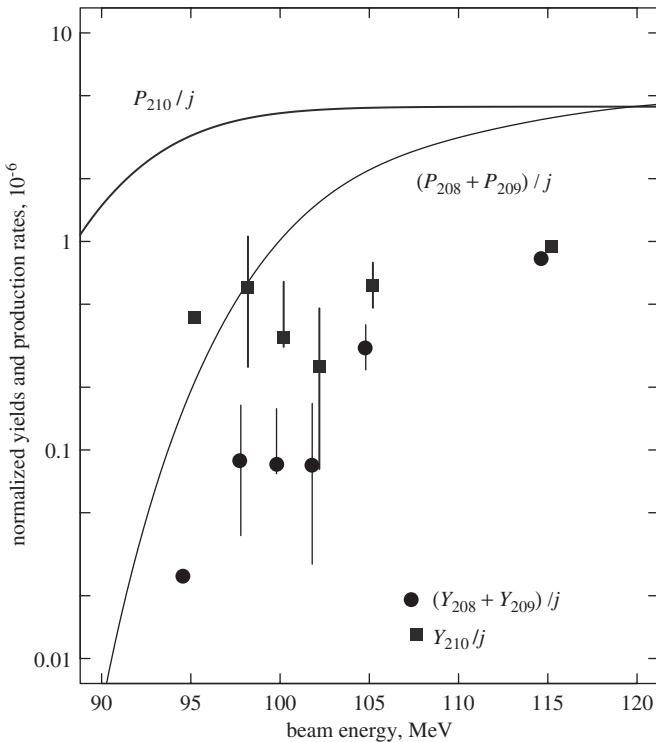

Fig. 7. ^{208,209}Fr (black circles) and ^{210}Fr (grey squares) normalized yields vs beam energy, for target temperatures above 1093 K. Estimated production rates (curves) are also shown for comparison.
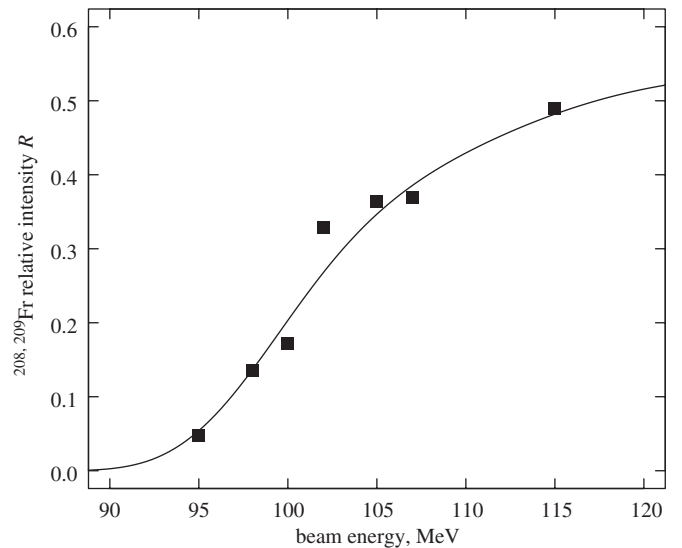

Fig. 8. Relative intensity of the observed ^{208,209}Fr peak: measured ratio R (squares) and predicted curve $R^{(\text{pred})}$ (line).
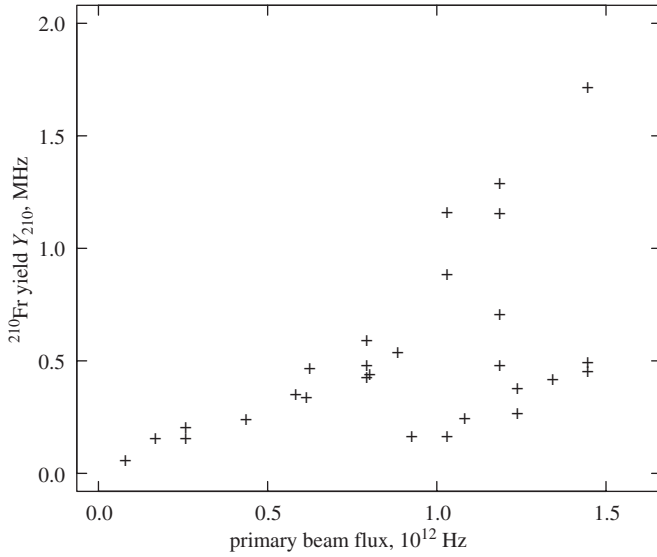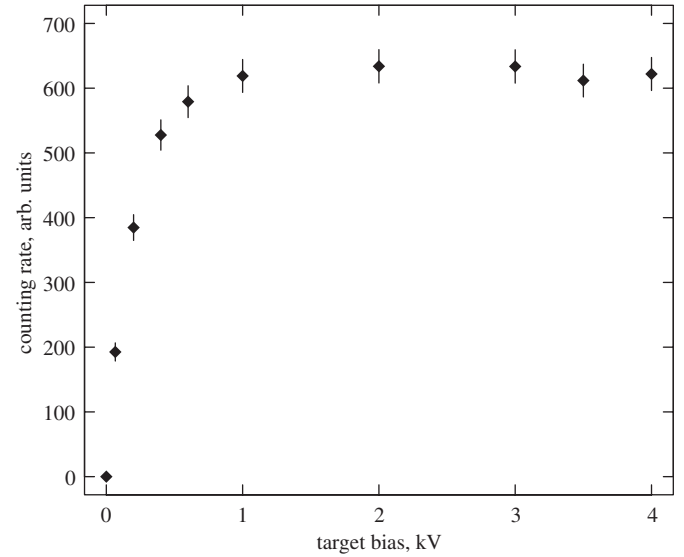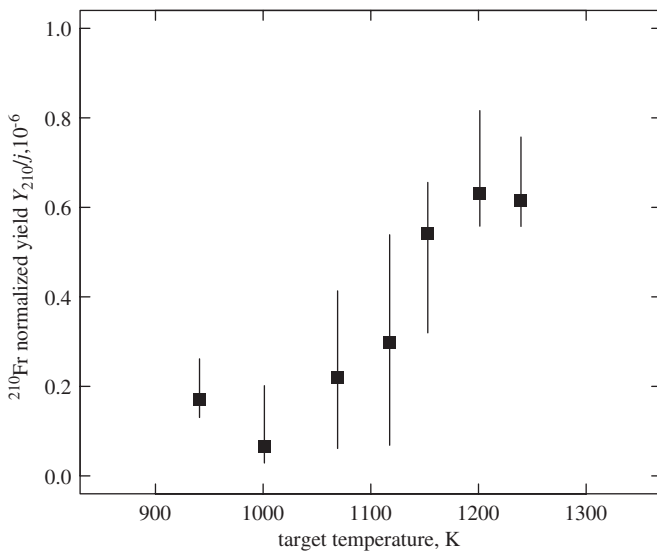
Fig. 9. ^{210}Fr yield vs beam flux.

Fig. 11. Event rate vs target voltage.

Fig. 10. Normalized ^{210}Fr yield vs target temperature.

The yield is proportional to the beam flux up to $j = 1 \times 10^{12}$ Hz. Fig. 9 shows data taken in the energy range $98\,\text{MeV} \leqslant E_0 \leqslant 107\,\text{MeV}$ and at temperatures in the interval $1193\,\text{K} \leqslant T \leqslant 1253\,\text{K}$. At higher fluxes, if one momentarily neglects some of the poorest targets, there appears to be a systematic increase in the slope, possibly due to beam-induced local melting. Fig. 9 also illustrates the dispersion of data from different targets.

To estimate the effect of bulk temperature, one can consider lower fluxes ($j \leqslant 10^{12}$ Hz) in the same energy range as above ($98\,\text{MeV} \leqslant E_0 \leqslant 107\,\text{MeV}$). The yield shows a sharp increase above 1100 K (Fig. 10).

The extraction electrode is designed to match the transport beam line (Section 4). The yield as a function of the target and electrode voltages is presented in Fig. 11.

Below 1 kV, there is an inefficiency mainly due to the ions not being sufficiently focused. At higher voltages all ions are injected into the beam line.

6. Conclusions

We have developed gold targets for the production of radioactive beams of francium in the mass range $208 \leqslant A \leqslant 211$. The most abundant isotope is ^{210}Fr with a maximum yield of 3×10^6 ions/s with a primary ^{18}O^{6+} 100 MeV beam flux of 1.5×10^{12} particles/s.

The average overall extraction efficiency is estimated to be about 15% under normal operating conditions and 40% when the target is locally melting. We attribute most of the inefficiency to the process of desorption from the target surface.

Since the primary beam power does not exceed 25 W, the design is kept simple and relatively inexpensive. Yields are reproducible to within a factor two, with a few targets being particularly good or bad. Possible reasons include mechanical and thermal nonuniformity, bulk or surface impurities, and primary-beam characteristics, but their contributions cannot be disentangled with the present setup.

References

[1] G.D. Sprouse, L.A. Orozco, Annu. Rev. Nucl. Part. Sci. 47 (1997) 429.
[2] W.C. Haxton, C.E. Wieman, Annu. Rev. Nucl. Part. Sci. 51 (2001) 261.
[3] V.A. Dzuba, V.V. Flambaum, O.P. Sushkov, Phys. Rev. A 51 (1995) 3454.
[4] J.L. Rosner, Phys. Rev. D 53 (1996) 2724.
[5] J.A. Behr, et al., Nucl. Instr. and Meth. A 351 (1994) 256.
[6] J.E. Simsarian, et al., Phys. Rev. Lett. 76 (1996) 3522.
[7] A.R. Lipski, et al., Nucl. Instr. and Meth. A 438 (1999) 217.
[8] J.M. Grossman, et al., Phys. Rev. A 62 (2000) 052507;
    J.M. Grossman, et al., Phys. Rev. A 62 (2000) 062502.

[9] A.R. Lipski, M.R. Pearson, Nucl. Instr. and Meth. A 480 (2002) 156.

[10] S. Aubin, et al., Rev. Sci. Instrum. 74 (2003) 4342.

[11] S.N. Atutov, et al., J. Opt. Soc. Am. B 20 (2003) 953.

[12] S.N. Atutov, et al., Phys. Scripta T105 (2003) 15.

[13] S.N. Atutov, et al., Hyperfine Interactions 146/147 (2003) 83.

[14] S.N. Atutov, et al., Nucl. Phys. A 746 (2004) 421.

[15] S.V. Andreev, V.I. Mishin, V.S. Letokhov, J. Opt. Soc. Am. B 5 (1988) 2190.

[16] Z.-T. Lu, et al., Phys. Rev. Lett. 79 (1997) 994.

[17] J.F. Ziegler, The Stopping and Ranges of Ions in Matter, vol. 5, Pergamon Press, Oxford, 1980.

[18] J.F. Ziegler, computer code SRIM, The stopping and range of ions in matter, IBM Research, 1996.

[19] W. Reisdorf, Z. Phys. A 300 (1981) 227.

[20] W. Reisdorf, M. Schädel, Z. Phys. A 343 (1992) 47.

[21] L. Corradi, et al., Phys. Rev. C 71 (2005) 014609.

[22] D.E. Eastman, Phys. Rev. B 2 (1970) 1.

[23] E. Arnold, et al., J. Phys. B 23 (1990) 3511.

[24] D.A. Dahl, Proceedings of the 43rd ASMS Conference on Mass Spectrometry and Allied Topics, Atlanta, Georgia, USA, 21–26 May 1995, p. 717.

[25] L.P. Ekström, R.B. Firestone, WWW table of radioactive isotopes, database version 28 February 1999 from <http://ie.lbl.gov/toi>.

[26] J. Streets, D. Slimmer, Fermilab computing division document PN540, <http://cddocs.fnal.gov/cfdocs/productsDB/docs.html>, July 2000.